Experimental and Numerical Study on Wall Impedance Effects on Tollmien–Schlichting Waves

Adrien Rouviere, Fabien Méry, Jeanne Methel, Olivier Vermeersch, Maxime Forte

Experimental and numerical study on wall impedance effects on TS waves

Adrien Rouviere*, Fabien Méry†, Jeanne Methel‡, Olivier Vermeersch§ and Maxime Forte¶
ONERA / DMPE, Federal University in Toulouse, F-31055 Toulouse, France

This paper investigates the effects of a porous wall on the development of Tollmien-Schlichting (TS) waves propagating inside a boundary layer. An experimental study performed in a low speed wind tunnel showed that micro-perforated panels over hollow chambers could promote laminar-turbulent transition. First, measurements of the streamwise evolution of the TS instabilities reveal that greater amplification occurs over perforated panels compared to a solid wall. This effect was attributed to a wall impedance condition imposed by the perforated panels over the chambers. This set-up is somewhat analogous to an acoustic liner for which the wall response is represented by a complex impedance. The impedance of the experimental set-up was thus measured *in situ*. These experimental impedance values were then used as wall boundary conditions of a linear local stability calculation to quantify the influence of wall impedance condition on TS wave growth. The e^N approach was applied to predict the corresponding transition positions. Comparison between experimental and numerical results shows that the use of impedance boundary conditions is a promising approach to predict transition location, particularly in the case of the panel with lowest resistance.

Nomenclature

t	=	time
x, y, z	=	streamwise, wall-normal and spanwise coordinates
c	=	speed of sound
ρ	=	density
$P, p', \hat{p}$	=	static pressure: mean, fluctuating and shape function of the fluctuating parts
$T, \theta', \hat{\theta}$	=	static temperature: mean, fluctuating and shape function of the fluctuating parts
$U, u', \hat{u}$	=	streamwise velocity: mean, fluctuating and shape function of the fluctuating parts
$V, v', \hat{v}$	=	normal velocity mean, fluctuating and shape function of the fluctuating parts

*PhD Student, DMPE, adrien.rouviere@onera.fr
†PhD, DMPE, fabien.mery@onera.fr
‡PhD, DMPE jeanne.methel@onera.fr
§PhD, DMPE, olivier.vermeersch@onera.fr
¶PhD, DMPE, maxime.forte@onera.fr

$W, w', \hat{w}$	=	spanwise velocity mean, fluctuating and shape function of the fluctuating parts
δ_1	=	boundary-layer displacement thickness
Re	=	Unit Reynolds number
Re_x	=	Reynolds number based on the distance from the leading edge
Re_{δ_1}	=	Reynolds number based on the displacement thickness
f	=	frequency of perturbation
ω	=	angular frequency: $\omega \stackrel{\text{def}}{=} 2\pi f$
F	=	reduced frequency of perturbation: $F \stackrel{\text{def}}{=} \frac{2\pi f^* \nu_e}{U_e^2} = \frac{\omega^* \nu_e}{U_e^2} = \frac{\omega}{\mathrm{Re}_{\delta_1}}$
$k = \omega/c$	=	wave number of the normal wave of the Kundt's tube
$\alpha_r + i\alpha_i$	=	longitudinal wave number
N	=	N factor: $N \stackrel{\text{def}}{=} \max_f \int_{x_0}^{x} -\alpha_i(f, \xi)\, \mathrm{d}\xi$
e	=	micro-perforated panel thickness
Φ	=	large hole diameter of the perforated panel
ϕ	=	small hole diameter of the perforated panel
σ	=	micro-perforated panel porosity
L	=	cavity depth
$Z = R + iX$	=	reduced impedance with its real part R as resistance term and its imaginary part X as reactance term
$Y = 1/Z$	=	reduced admittance
$\cdot^*$	=	physical quantity (opposite to dimensionless)
$\cdot'$	=	fluctuating component
$\hat{\cdot}$	=	shape function of the fluctuation (only y-dependant)
$\cdot_\infty$	=	incoming flow
$\cdot_{\mathrm{rms}}$	=	root mean square value
$\cdot_e$	=	external (to the boundary layer) flow
$\cdot_0$	=	inside the cavity
LST	=	Linear Stability Theory
PSD	=	Power Spectral Density

I. Introduction

The study of the laminar-turbulent transition is an active field of research in the aerospace industry. While its main objective is to reduce skin-friction drag, and therefore fuel consumption, various strategies can be implemented to delay this transition. In particular, one solution involves applying suction through a micro-perforated sheet mounted over a

suction plenum. Another facet of transition control is to predict correctly the onset of transition: the e^N method [1, 2] is one of the most efficient and relatively simple tools currently available. In this method, the N factor represents the amplification of the boundary layer instabilities (in our 2D incompressible case, the Tollmien-Schlichting (TS) waves) and transition is assumed to occur when the N factor reaches a critical value N_T.

In 1998, in-flight transition measurements [3] on an A320 vertical tail plane integrating suction control through a titanium micro-drilled panel showed that the critical N factor for boundary layer instabilities was reduced compared to natural laminar flow configurations (*i.e.* solid wall). These results indicated that despite the globally stabilizing effect of wall suction to control transition, a destabilizing phenomenon existed. It was first attributed to either: non-homogeneous mean flow due to suction being applied through localized discrete hole, and/or a distributed 'roughness' effect introduced by the holes, and/or a noise generated by the suction system [4]. In this paper, we propose and substantiate an alternative explanation based on a wall impedance condition. As a first attempt, this study focuses on a boundary layer developing above perforated panels without any suction velocity. In this paper, we present experimental results in a low speed wind tunnel that show how such a set-up (micro-perforated panel over cavity with no suction) can actually promote transition, compared to a solid wall configuration.

Some experiments [5] indicate that such a mechanism can be due to a modification of the wall boundary condition. A micro-perforated panel over the suction chambers can crudely be compared to an acoustic liner, designated as SDOF (Single Degree Of Freedom). These SDOF liners are used to reduce the noise emitted by a guided environment (turbojet engine nacelle, air duct, automobile exhaust ...) and typically consist of a thin material (resistive layer) glued on partitioned air cavities (honeycomb structure) with a rigid backplate. The working principle behind conventional acoustic liners is that of Helmholtz resonators: acoustic energy is converted to turbulent fluid motion and thermal energy due to the action of the induced periodic in- and outflow and viscous effects, which can be modeled as an impedance boundary condition. The impedance of such a configuration can be measured [6] and modeled [7–11].

Several numerical studies recognized the interaction between the boundary-layer flow and a passive porous surface. The term "passive" refers to a surface through which neither suction nor blowing is imposed since the mean pressure value is assumed to be the same on both sides of the porous panel. Burden [12] demonstrated using linear stability theory (LST) that an impedance wall condition could destabilized the laminar boundary layer. He suggested that the local velocity fluctuations through the wall (v') tended to add themselves to the fluctuations already present in the boundary-layer resulting in an increase of the Reynolds stresses.

Gaponov [13], still using LST showed that a non-zero normal velocity fluctuation at the wall decreased the critical Reynolds number *i.e.* the Reynolds number below which all disturbances are damped.

Lekoudis [14] computed the linear growth rate of the instability waves propagating above a perforated plate mounted over chamber(s). He characterized the influence of the permeable surface on the flow as an admittance (inverse of impedance) boundary condition whose values depended on the geometric parameters of the configuration, in particular

the volume of the chamber beneath the perforated plate. Two configurations were considered: the first one including a single large chamber and the other consisting of several small chambers with a limited extent in the chordwise direction. The latter (small chambers) had no effect on the boundary layer stability while the former (single large chamber) could significantly reduce the amplification of Tollmien-Schlichting instabilities. Lekoudis suggested that fluctuating pressure field from the TS waves at the wall forced air through the perforations, which led to a reduction of the energy production from the Reynolds stresses.

More recently, Carpenter and Porter [15] studied the ability of passive porous walls in delaying the transition onset. The authors noticed that wall admittance is complex, meaning that the flow through the perforations is usually out of phase with the driving pressure that the TS waves generate as they push flow through the porous wall. Although the main purpose of the article was to determine some of the key parameters for a porous wall to have a stabilizing effect, the authors found that in most cases, a porous wall resulted in a higher disturbance growth rate compared to the one of impermeable surfaces.

In 2015, Tilton and Cortelezzi [16] solved the mean flow and perturbation equations both in the boundary layer and the porous material using a volume-average approach so that the permeability and the porosity explicitly appear in the equations. They demonstrated that permeability significantly broadened the range of unstable frequencies, and enlarged the local growth rate value.

Choudhari [17] theoretically studied the influence of a localized non-zero (but low) surface admittance on both the receptivity and the stability of a boundary layer. Considering the first phenomenon, non-zero admittance surface is an efficient wavelength conversion site from external acoustic disturbances to TS-like instabilities. In particular, this receptivity mechanism becomes more efficient as the start of the non-zero admittance region moves closer to the neutral point, past which TS instabilities start to amplify (see [18]). A non-zero admittance surface can also modify the stability of TS waves. Indeed, a short scale variation in wall admittance distribution will lead to a scattering of the TS wave that were generated upstream. A part of the scattered field consists of this incident TS wave itself so that the instability wave in the region downstream is determined by the interference between the primary (incident) wave and the secondary wave originating from the scattering. The two (receptivity and stability) phenomenons are thus related since the scattering region can be seen as a source of receptivity not to external acoustic fluctuations but to the Tollmien-Schlichting waves propagating inside the boundary-layer. Choudhari demonstrated that for wall impedances that were resistance-dominated (real values) had a more destabilizing effect than reactance-dominated wall impedance (imaginary values). He also noticed the specific influence of non-zero surface admittance in the modification of Reynolds stresses in the near-wall region confirming the hypothesis of Burden [12].

All these numerical and theoretical results tend to indicate that there is a significant effect of a passive porous wall on the boundary layer stability and thus on the laminar to turbulent transition process. Regardless of whether or not this effect could be used as a passive flow control technique, understanding the interaction between boundary-layer flow and

porous wall seems to be one area of investigation which could help improve transition prediction models for Hybrid Laminar Flow Control (HLFC) purpose.

In the first part of this paper, the experimental set up and the measurements of a flow over a flat plate that includes a perforated panel is presented. To the best of the authors knowledge, these experimental data, showing a non-negligible effect of a porous wall on boundary layer transition at low velocity, are the first measurements to be published in the open literature. The measurements of TS amplification as well as transition location for two different perforated panels are presented and compared to the reference impermeable surface configuration. The measurement of the impedance of the set-up is performed through a portable impedance tube device. In the second part, a numerical approach based on the combined use of a boundary layer parabolic solver with a linear local stability code integrating an impedance boundary condition representative of the experimental set-up is briefly introduced. The amplification of TS waves and the transition location prediction (e^N method, [1, 2]) are then computed with and without a wall impedance condition. Finally, the numerical results are compared with the measurements to provide some initial validation about using impedance boundary conditions to model the destabilizing effect of a perforated panel mounted over a hollow chamber on TS waves.

II. Experimental set-up and flow measurements

A. Flat plate flow over micro-perforated panels : experimental set-up

The experimental facility is briefly described in this section but more details can be found in [5]. The present investigation was performed in an open-return subsonic wind-tunnel operating at local atmospheric conditions. All tests were performed at a single nominal unit Reynolds number, $2.6 \times 10^6\ \mathrm{m}^{-1}$, which corresponds to approximately $40\ \mathrm{m\,s}^{-1}$.

The perforated panels were mounted on a flat plate model, as shown in Figure 1, over nine plenum chambers. The aluminum flat plate is 0.035 m-thick by 0.400 m-wide, and has a total length (from leading to trailing edges) of 1.10 m. The panels can be inserted 0.18 m from the leading edge over nine chambers, each having dimensions 0.048 m (streamwise length, x) by 0.019 m (depth, y) by 0.350 m (spanwise width, z) and separated by 0.002 m-thick stringers, which results in a total streamwise length of 0.450 m.

This set up was initially intended to study wall suction effects on transition [5]. In the present paper, all the results were obtained without suction, with all flow meter valves shut to prevent any passive suction or blowing in the chambers.The shaded area, labeled "velocity measurement area" on Figure 1 corresponds to the centerline region in which single-wire hotwire anemometry measurements were performed using a Dantec Streamline and a 55P15 probe. For each measurement, 200 000 samples were acquired at 25 kHz. The two main types of measurements were: boundary layer profiles and streamwise traverses at a constant height from the flat plate wall. This constant height

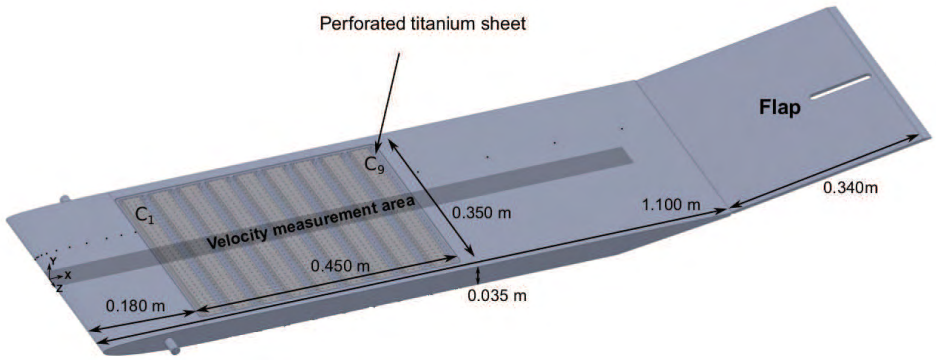

Fig. 1 General layout of the flat plate and flap with details on the perforated region.

was chosen in order to probe the boundary layer where the maximum velocity fluctuations could be found (as can be seen in Figure 5), thereby providing increased sensitivity to the onset of the first turbulent spots and transition. These streamwise traverses were used to determine the transition position, which corresponds to the position where the slope of the signal is first equal to or greater than a given threshold. Hot-wire measurement uncertainty is discussed and quantified in the Appendix V.A.

B. Characteristics of micro-perforated sheets

The three panels consist of one 0.9 mm-thick solid aluminum panel and two 0.9 mm-thick micro-perforated titanium sheets, flush-mounted with the rest of the flat plate's upper side. Perforations were obtained using laser micro-drilling, which results in an unintentional conical cross-section for the perforations characterized by different inner Φ and outer ϕ diameters. After manufacturing, these average values were determined by statistical post processing of the data provided by a light transmission control technique, developed at ONERA and discussed in [19]. In order to avoid hole blockage by any dust particles advected by the flow, the face corresponding to the smallest radius is the one in contact with the flow. The panel P_1 has a 92 µm-outer-diameter holes evenly spaced in a square pattern of dimensions 1.6 mm × 1.6 mm corresponding to a porosity* of 0.26%. The panel P_2 has 188 µm-diameter holes evenly spaced in a square pattern of dimensions 1.44 mm × 1.44 mm resulting in a 1.34% porosity. The characteristics of the perforated plates are shown schematically in Figure 2 and reported in Table 1. In the experimental set-up, the perforated panel extends from 180 mm to 630 mm.

*the porosity is defined as the ratio of the hole's area to the sheet's total surface area

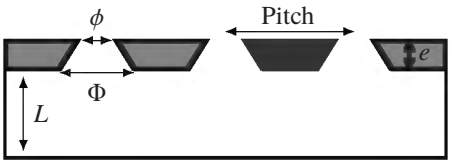

Fig. 2 Geometry of the micro-perforated panel and the plenum.

Panel	σ [%]	ϕ [µm]	Φ [µm]	e [mm]	L [mm]	Pitch [mm]
P_0	0	-	-	0.9	-	-
P_1	0.26	92	146	0.9	19	1.6
P_2	1.34	188	202	0.9	19	1.44

Table 1 Geometry of the micro-perforated panels.

C. Effect on laminar-turbulent transition

The transition locations for different combinations of a micro-perforated panel over plenum chambers are compared to that of a rigid hard wall in Figure 3. This figure represents the spatial evolution of the rms value of the streamwise velocity fluctuation u'_{rms} non-dimensionalized by the upstream mean velocity U_∞: to obtain these measurements, the hot-wire is traversed in the streamwise direction from the leading edge at a constant distance from the wall $y = 300\,\mu$m in the boundary layer. The transition onset occurs at the location where the abrupt increase in the rms value of the velocity fluctuation is equal to or greater than $2 \times 10^{-4}\,\mathrm{mm}^{-1}$ and subsequently continues to increase; this increase corresponds to the appearance of the first near-wall turbulence spots. The uncertainty in the transition position is discussed in appendix V.A (see Figure 15), and, given the present approach, is ±15 mm.

On Figure 3, the transition position for the solid wall panel (P_0, reference configuration) is approximately 740 mm from the leading edge, corresponding to $\mathrm{Re}_{x_T} = 1.92 \times 10^6$ in terms of streamwise Reynolds number. The dotted curves labelled P_1 (blue) and P_2 (green) show that the transition position moves upstream, respectively to $\mathrm{Re}_{x_T} = 1.63 \times 10^6$ ($x_T = 630$ mm) and $\mathrm{Re}_{x_T} = 1.32 \times 10^6$ ($x_T = 510$ mm), indicating a destabilizing effect from the perforated walls.

In the experimental set-up, as mentioned previously, the suction system (*i.e.* the pump) is turned off so that no parasitic noise exists. To verify that this destabilizing effect was not related to the distributed roughness of the perforations either, tape was applied on the bottom surface of panels P_1 and P_2 so that the boundary layer was still in contact with the perforations but could not communicate with the chambers. Based on this test, the transition positions for the taped perforated panels recovered that of the solid wall panel, as shown by the curves labeled "P_1 taped below" and "P_2 taped below" on Figure 3. The destabilizing effect from panels P_1 and P_2 on the boundary layer cannot therefore be attributed to a distributed roughness effect from the perforations.

The observed effect could potentially be related to modifications to the receptivity or the amplification of the TS instabilities (which are the instabilities driving transition in the case of the solid wall panel). In an attempt to understand which (if any or both) of the two phenomena was occurring, the power spectral densities of the hot-wire signal obtained at $y = 300\,\mu$m from the wall and at several streamwise locations for the boundary layer developing above the three

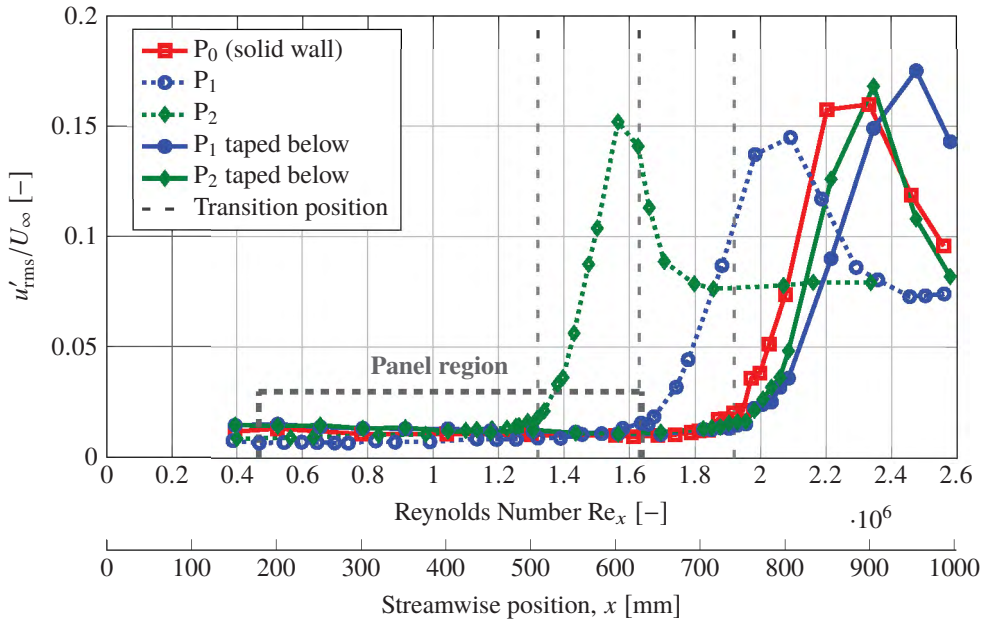

Fig. 3 Hot wire measurements: rms value of the streamwise velocity fluctuations at $y = 300\,\mu$m from the wall. Determination of the transition positions for all panels.

panels are plotted in Figure 4(b).

Since hot-wire measurements are time-resolved, the analysis of the velocity fluctuations inside the boundary layer allows the identification of the most amplified frequencies, as shown in Figure 4(a). In this figure, the spectral analysis is shown at different streamwise positions located just upstream of the respective transition locations where the instabilities responsible for transition are sufficiently amplified to be identified in terms of frequency. The streamwise positions are indicated in the figure's legend. The boxed region in Figure 4(a) zooms over the most amplified TS wave frequencies (400 Hz to 1 kHz), which are centered around approximately 600 Hz, regardless of the porosity. The three PSD have very similar overall shapes, despite their different absolute streamwise positions, possibly indicating that the transition mechanism is not modified but simply accelerated.

This hypothesis is also supported by Figure 4(b), where the PSD for all three panels are compared at the same altitude ($y = 300\,\mu$m) inside the boundary layer and at the same streamwise position ($x = 508$ mm from the leading edge). Over the range of frequencies previously determined to be the instabilities responsible for transition, the P_2 case, which transitions the earliest, has significantly greater amplitude than in the case of either P_0 or P_1. The fact that the amplified frequency range seems unchanged and that panel P_2 has the largest instability amplitudes seem to strongly suggest that wall impedance does not change the fundamental transition mechanism but rather affect the instabilities' amplification.

To further investigate this phenomenon, the PSD of u' is calculated for each measured point of a boundary layer profile, and then integrated over a frequency band ranging 40 Hz, centered on the frequency of interest. Finally, to revert

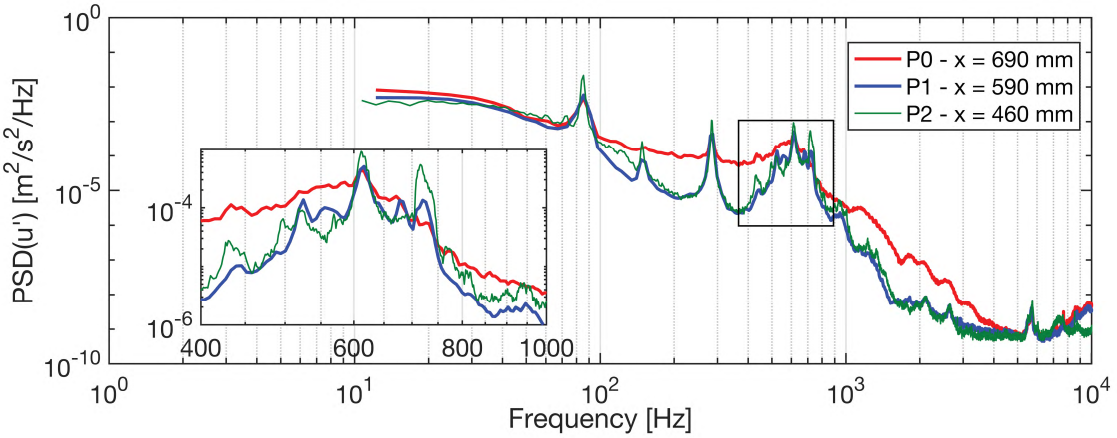

(a) Positions upstream of the transition onset where TS waves are visibly amplified

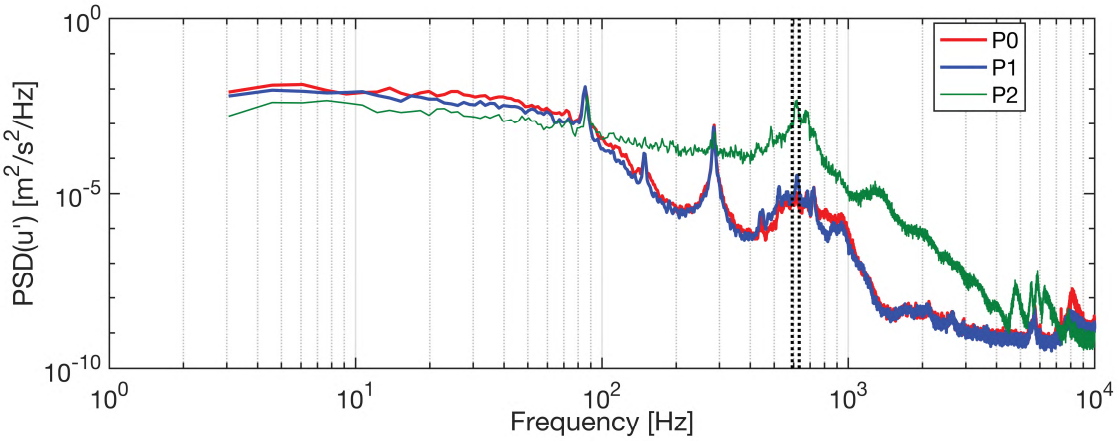

(b) At $x \approx 508$ mm from the leading edge ($\mathrm{Re}_x = 1.32 \times 10^6$) with limits of integration of the velocity fluctuation profiles

Fig. 4 Power Spectral density (PSD) of the streamwise velocity fluctuation at $y = 300$ µm from the wall

to units of velocity, the square root of these computed values is taken and the corresponding quantity is labeled $u'_{\mathrm{rms},\Delta f}$. In this study, the frequency range of integration was set to 592 – 632 Hz for all panels and is shown by the dotted black lines in Figure 4(b). Using this method, the $u'_{\mathrm{rms},\Delta f}$ profiles at different streamwise locations are extracted, as shown in Figure 5. On this figure, the shape function of Tollmien-Schlichting waves computed using linear stability theory (see paragraph IV.A) have been added for comparison. For all three panels these profiles are generally found to correspond well to TS instability profiles, and therefore the same transition mechanism.

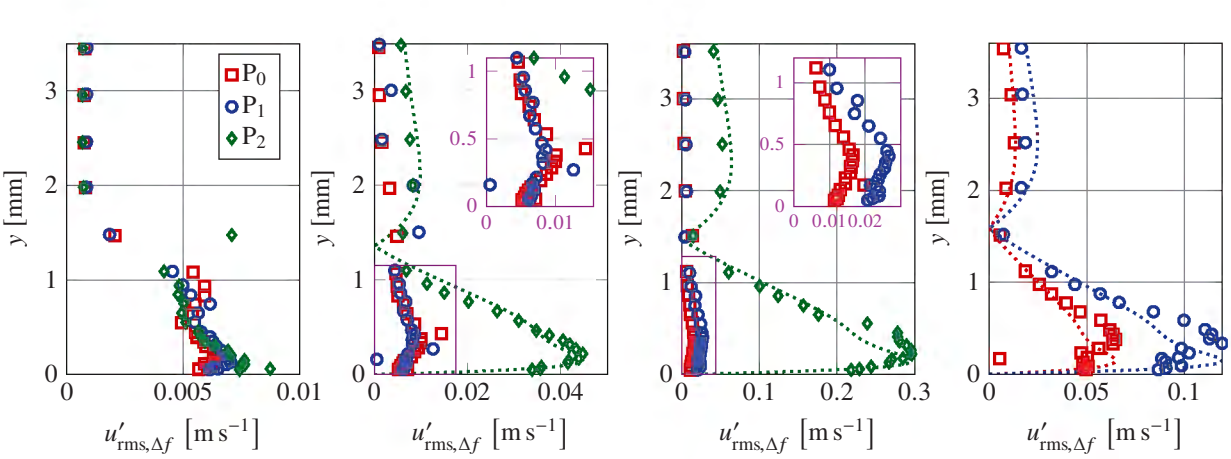

(a) $\mathrm{Re}_x = 5.3 \times 10^5$, $x = 208$ mm, C1 **(b)** $\mathrm{Re}_x = 1.1 \times 10^6$, $x = 408$ mm, C5 **(c)** $\mathrm{Re}_x = 1.3 \times 10^6$, $x = 508$ mm, C7 **(d)** $\mathrm{Re}_x = 1.6 \times 10^6$, $x = 608$ mm, C9

Fig. 5 Streamwise evolution of velocity fluctuation profiles evaluated over frequency range [592 – 632] Hz for all panels. Symbols: measurements, Lines: shape function of Tollmien-Schlichting waves from linear stability theory

The first streamwise position, shown in Figure 5(a) is centered over the first chamber of the plenum. At this location, all $u'_{\mathrm{rms},\Delta f}$ profiles have similar shapes and comparable magnitudes, despite the abrupt change in wall impedance for cases P_1 and P_2. The corresponding mean flow velocity profiles are shown in Figure 6(a) and are similar to a Blasius theoretical shape. At the next streamwise position $x = 408$ mm, shown in Figure 5(b), the $u'_{\mathrm{rms},\Delta f}$ profile for the P_2 panel first starts to have slightly greater amplitude than the other two profiles, and exhibits the pronounced features of a fully developed Tollmien-Schlichting instability profile.

At the next position (Figure 5(c)), located immediately upstream of the P_2 transition location, the $u'_{\mathrm{rms},\Delta f}$ profile for P_2 has undergone even greater amplification while the P_0 and P_1 profiles still have significantly lower magnitudes. Additionally, the $u'_{\mathrm{rms},\Delta f}$ profile for panel P_1 now has slightly greater amplitude than the P_0 solid wall case, as shown in the inset graph. This last trend is further amplified in Figure 5(d), where the maximum amplitude of the $u'_{\mathrm{rms},\Delta f}$ profile for panel P_1 is now approximately twice that of panel P_0. The $u'_{\mathrm{rms},\Delta f}$ profile for P_2 panel is no longer shown since the corresponding boundary layer is almost fully turbulent. This is confirmed by the mean velocity profile (green diamonds

in Figure 6(b)), while boundary layers over P_0 and P_1 panels still remain laminar as shown by the comparison to the Blasius theoretical shape.

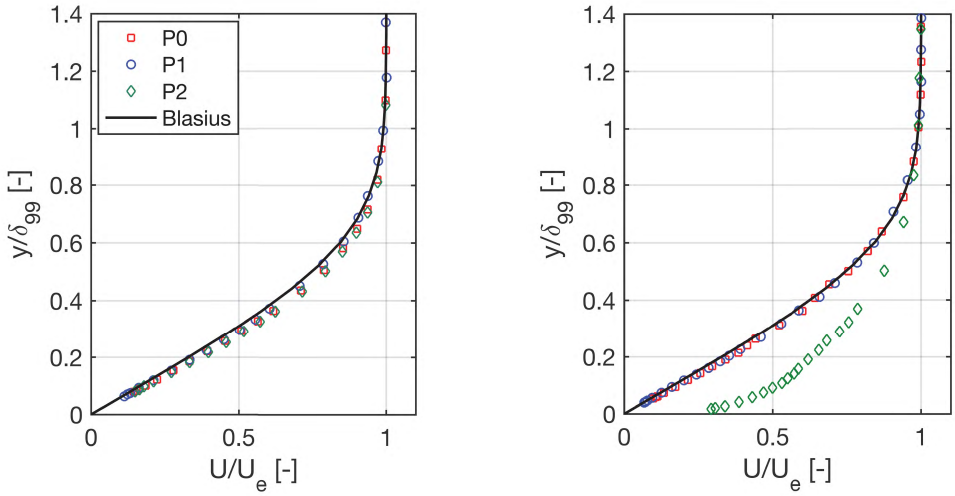

(a) $\mathrm{Re}_x = 5.3 \times 10^5$, $x = 208$ mm, C1 **(b) $\mathrm{Re}_x = 1.6 \times 10^6$, $x = 608$ mm, C9**

Fig. 6 Hot wire measurements: mean flow velocity profiles.

The streamwise evolution of the maxima of the fluctuation $u'_{\mathrm{rms},\Delta f}$ profiles (still evaluated over the frequency range $\Delta f = [592 - 632]$ Hz) is given for each suction panel in Figure 7. Over the first three suction chambers, the amplitudes are comparable, regardless of the panel. Beginning at the fourth streamwise position, the P_2 maximum amplitudes depart from the two other panels, and start to increase significantly until transition is detected close to $\mathrm{Re}_{x_T} = 1.32 \times 10^6$ ($x_T = 510$ mm). The difference between panels P_0 and P_1 becomes noticeable over the sixth suction chamber, after which each data set seems to amplify at a different rate. These results provide evidence in favor of the hypothesis that the porous panel mainly affects the amplification of instabilities.

III. Impedance characterization of the micro-perforated panels

A. Impedance formulation

The combination of a micro-perforated panel mounted over a plenum therefore seems to affect boundary layer stability through an effect that is not related to the panel's surface roughness nor external noise sources such as a suction pump. This configuration could crudely be modelled by a Single Degree of Freedom (SDOF) liner. Although the chambers have a much larger plenum volume than any typical honeycomb structure, the similarities between liners and the present configurations, as will be shown in this section, are compelling enough to allow the use of a liner model to perform the following numerical investigation. The interactions that can occur between the hydrodynamic perturbations found in the boundary layer and this liner-type surface are mainly governed by the surface's opposition to the flow. If the surface is porous, some absorption can occur: the interaction can therefore be modelled by a wall impedance boundary

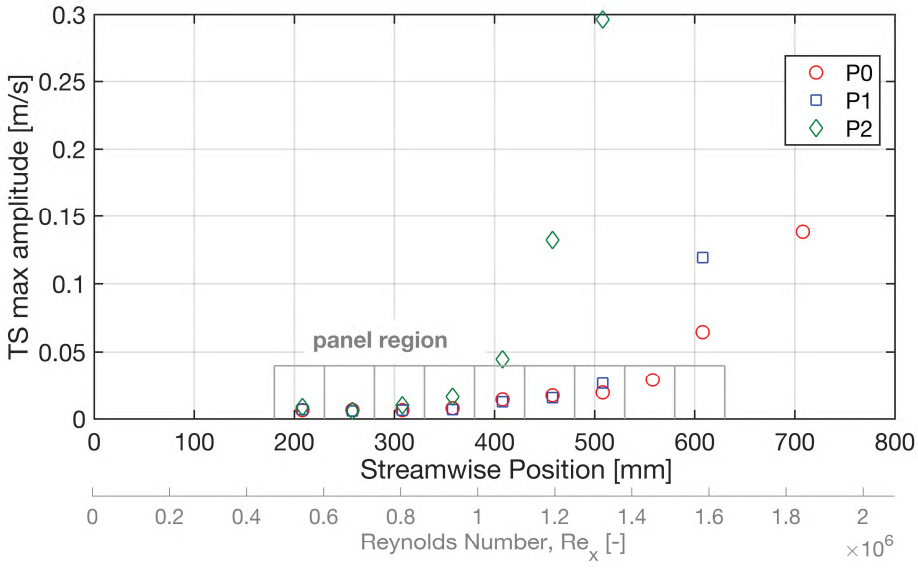

Fig. 7 Streamwise evolution of the u' profile (evaluated over Δf = [592 – 632] Hz) maximum amplitude for the three panels.

condition.

Recently, Gabard [20] proposed an acoustic impedance definition in the general case of viscous fluid. This generalized impedance Z_g relates the strains at the wall to the velocity vector through:

$$Z_g = \begin{bmatrix} Z_{tt} & Z_{nt} \\ Z_{nt} & Z_{nn} \end{bmatrix} \tag{1}$$

and

$$\begin{pmatrix} \tau'_{nt} \\ p' - \tau'_{nn} \end{pmatrix} = Z_g \cdot \begin{pmatrix} u' \\ v' \end{pmatrix} \tag{2}$$

where $\cdot'$ represents fluctuations with respect to the base flow and τ the corresponding viscous stress tensor. This impedance formulation is not so easy to evaluate since viscous terms from the stress tensor are difficult to assess experimentally. The standard impedance condition can be recovered by neglecting the viscous component and thus $Z_{nt} = Z_{tt} = 0$. This assumption appears to be reasonable in the case of a locally reacting SDOF liner, which is correct in the present case, leading to a direct proportionality at the wall between pressure and normal velocity through $p' = Z_{nn} \cdot v'$. To simplify the notation the impedance Z_{nn} will be referred as $Z(\omega)$ and is the complex wall impedance (inverse of the admittance $Y(\omega)$) and depends on the frequency which can be expressed as:

$$Z(\omega) = \frac{1}{Y(\omega)} = \frac{p'(\omega)}{\rho_0 \cdot c_0 \cdot v'(\omega)} = R(\omega) + iX(\omega) = |Z|(\omega) \cdot e^{i\varphi(\omega)}, \tag{3}$$

with $\omega = 2\pi f$, the angular frequency, p' the fluctuating pressure at a point on the surface, v' the normal fluctuating velocity at that point, ρ_0 the fluid density and c_0 the speed of sound in the resting medium. This non-dimensionalization corresponds to an acoustic approach. The implicit time dependence convention used in this article is $\exp(i\omega t)$.

The real part of the impedance R is called the resistance and is mostly imposed by the geometrical properties of the perforated panel. Gabard [20] demonstrated that due to the passivity principle, stating that the wall surface receives more energy than it provides to the fluid, R must remain positive. Its imaginary part X, the reactance, is largely dictated by the cavity itself. In the numerical section (section IV.A), the contribution of each of these terms on the stability of Tollmien-Schlichting waves will be qualitatively studied on the flat plate Blasius boundary layer case. In certain cases, the wall properties will be expressed as an admittance value Y.

B. Principle behind and instrumentation for impedance measurement

Although the present configuration is analogous to a liner, the low porosity panels and the hollow chambers make for an atypical type of liner. Existing methods to evaluate the impedance based on a typical SDOF liner's properties might therefore not be applicable. For this reason, the impedance of the set-up was evaluated by performing *in situ* measurements using a portable impedance tube presented in this section. This *in situ* approach enables a measurement representative of the real mock up.

The impedance characterization in the normal wave incidence condition is based on the Chung and Blaser [6] transfer function method using two microphones. The sound pressure is measured at two locations on the Kundt's tube (*i.e.* an impedance tube, schematically depicted in Figure 8(a)) and the reflection coefficient $\beta(\omega)$ can be derived:

$$\beta(\omega) = \frac{1 - Z(\omega)}{1 + Z(\omega)} = \frac{H - \mathrm{e}^{+iks}}{\mathrm{e}^{-iks} - H} \mathrm{e}^{-2ik(\ell+s)}, \tag{4}$$

where H is the transfer function between the two microphones, ℓ the distance between the first microphone and the sample, $k = \frac{\omega}{c}$, the wave number of the normal wave and s the distance between the two microphones.

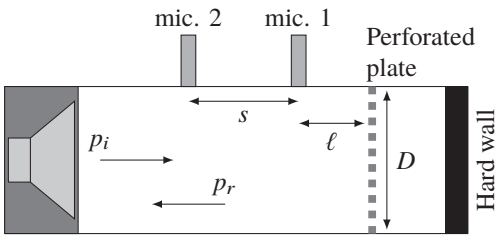

(a) Schematic view of an impedance tube with a loud speaker.

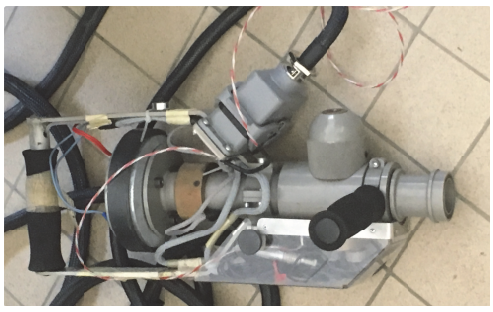

(b) Airbus portable impedance tube.

Fig. 8 Impedance measurement: principle and instrumentation.

In order to quantify the properties of nacelle liners at the output of the assembly line, Airbus developed and manufactured a portable impedance measuring device, as shown in Figure 8(b). Thanks to this device, *in situ* measurements of the impedance of the experimental set-up were performed (thereby taking into account the effective combination of the perforated plate and chambers). The diameter of the device's tube is $D = 30$ mm and the microphones are paired in order to minimize phase error. Before each measurement, the device is calibrated (the distances ℓ and s are recalculated from a rigid sample). The measurement is corrected for temperature effects and the device is tested on a reference liner sample (reference SDOF). The device is verified when the uncertainty on the resistance of the reference liner sample for a frequency range of 1500–3000 Hz is less than ±2% and the educed depth error of the honeycomb is less than ±1%. This guarantees an extended measurement uncertainty less than ±2% on the reflection coefficient $\beta(\omega)$. These measurements do not take into account the effect of the grazing flow, which tends to slightly increase the resistance [8, 21]. Whereas the low porosity effect should increase the effect of the grazing flow, the small size of the holes should minimize this increase [22].

Further experiments on a dedicated sample in a specific bench [23] should be performed to precisely evaluate the grazing flow effect.

C. Impedance measurement results

In this section, the normalised *in situ* measurements from the portable impedance device mentioned in the previous section are presented and shown in Figures 9 and 10. The impedance measurements were performed on the entire device with a white noise acoustic excitation at a Sound Pressure Level of 110 dB. The 95% confidence interval is also plotted in order to evaluate the accuracy of the measurement.

Several repeatability measurements have been performed at several location to ensure the robustness of the result in the frequency bandwidth of interest (from 500 Hz up to 1000 Hz), corresponding to the typical frequencies of the TS waves involved in this configuration. At higher frequency, discrepancies become significant.

This type of measurement is most relevant to acoustic liners, where the normal absorption is usually high for a given sound pressure level. It is clear that the results highlight a reflexive configuration contrary to an optimized acoustic liner. Particularly, the P_1 panel exhibits a very high resistance level (Figure 9(a)), behaving similarly to a rigid wall. For an acoustic application, the set-up would be considered a hard wall. The reactance curve differs from a classical Helhmholtz resonator reactance trend, which was expected since the plenum was not partitioned in the spanwise z-direction. The low normal absorption makes the measurement very sensitive, especially with respect to the phase, which is a key parameter for the reactance value. For panel P_2, the resistance, shown in Figure 10(a), is significantly lower. The set-up cannot be considered as locally reacting. Nonetheless, for the panel P_2, on Figure 10, the reactance trend seems similar to a classical SDOF acoustic liner and behaves as an Helmholtz resonator according to $X = \text{cotan}\,(kL)$ (with $k = \omega/c$ and L the plenum depth). During the impedance measurements, partitions were added in

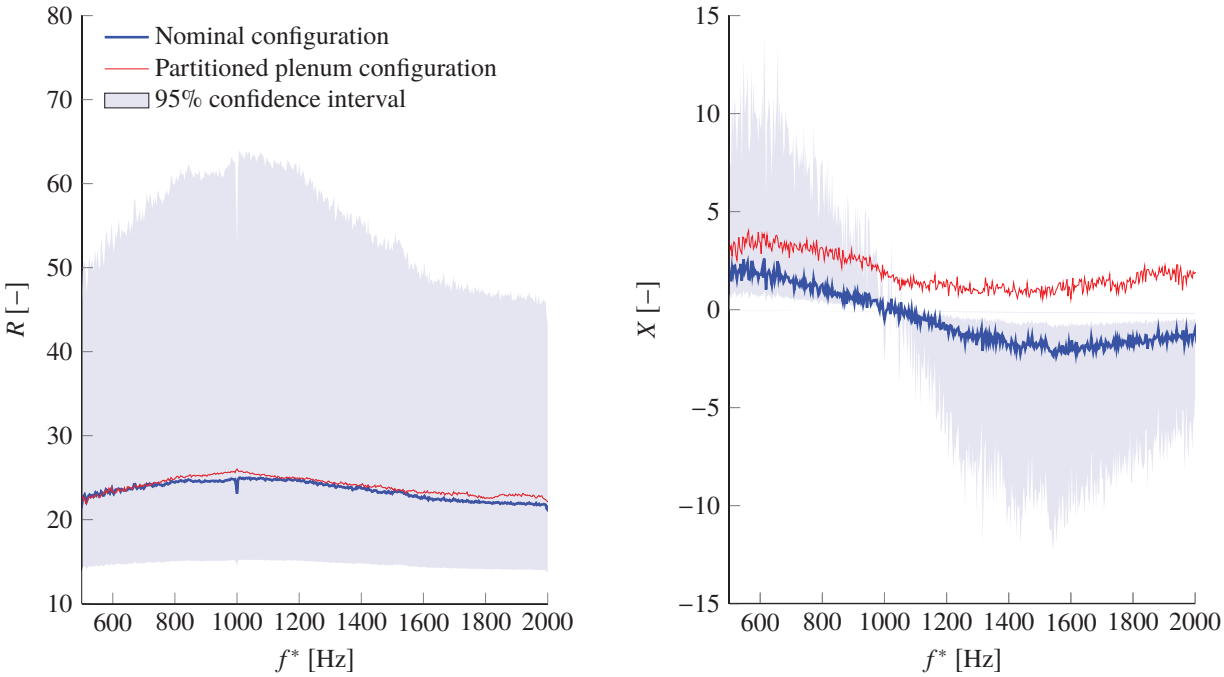

(a) Normalised Resistance **(b) Normalised Reactance**

Fig. 9 Portable device impedance result with 95% confidence interval of the perforated panel P_1.

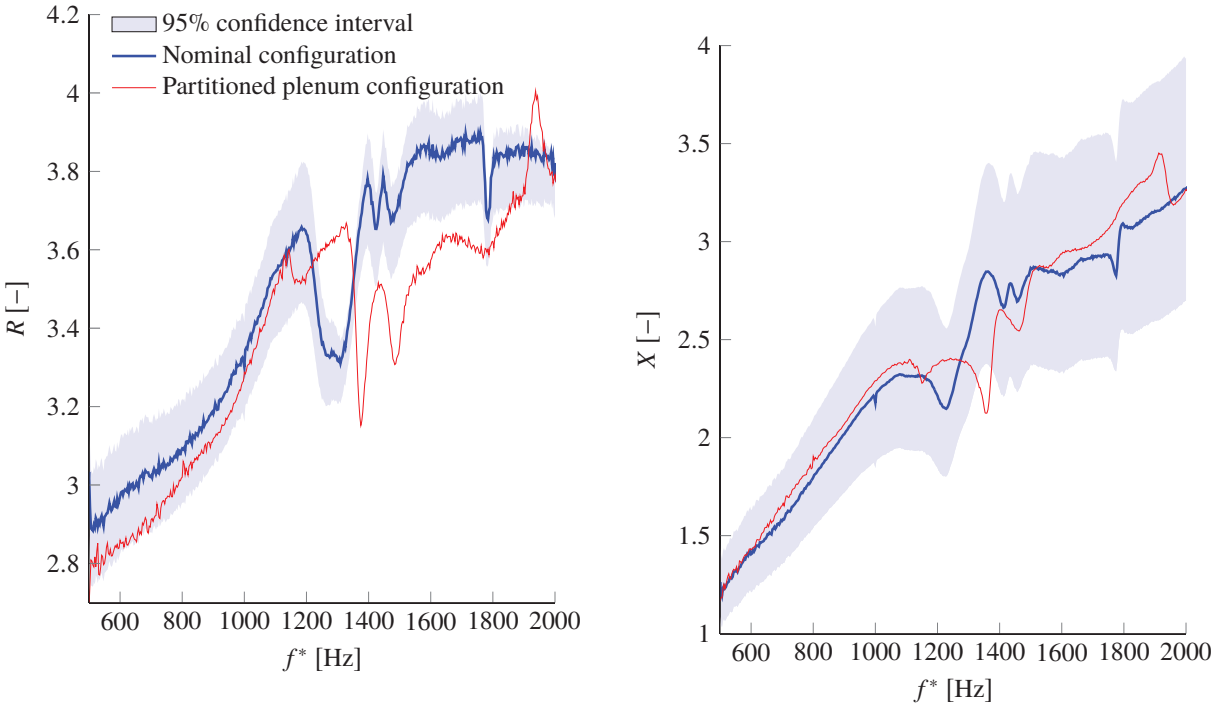

(a) Normalised Resistance **(b) Normalised Reactance**

Fig. 10 Portable device impedance result with 95% confidence interval of the perforated panel P_2.

order to assess the locally-reacting assumption: small plastic barriers were introduced in order to have square partitions compatible with the impedance tube aperture (at least 4 partitions). Several measurements were performed cautiously and repeatedly on different partitioned area in order to ensure the quality of the results (avoiding any spurious results due to leakage). The partitions enable to ensure the locally-reacting assumption but are incompatible with the nominal configuration dedicated to HLFC configuration studies. The effect of these partitions is highlighted with the red lines in the Figures 10 and 9, and the discrepancies with the nominal configuration remain weak in the frequency bandwidth of interest. In short, for P_2, the set-up can be considered as locally reacting only on a restricted frequency bandwidth, from low frequency up to around 1200 Hz: the partitioned configuration remain in the uncertainty of the measurement with the nominal configuration (plenum free from partitions). For P_1, the partition seems to have a negligible impact on the resistance results.

In the first part of this paper, a boundary layer developing over a porous wall was found to transition earlier than over a solid wall. Additional tests led to the hypothesis that this effect could be the result of an impedance boundary condition at the wall. Thus, the impedance of the two perforated panels mounted above plenum chambers was measured. In order to further validate the hypothesis, a numerical analysis is presented in the following section. It is based on a classical linear stability approach able to quantify the amplification of boundary layer instabilities; however, the classical impervious fixed wall condition $v' = 0$ is changed into a wall impedance condition $v' = \frac{1}{Z_{\text{stab}}(\omega)} \cdot p'$ coupling the pressure and normal velocity fluctuation at the wall. The impedance value (depending of the frequency) is deduced from the measurements presented in the present section. The impedance measurement suffers from several uncertainties due to the high resistive configuration (due to the hole size and the low percentage of open area) and the large plenum below the perforated panels. This configuration remains unconventionnal compared to classical acoustic single degree of freedom liner characterisation. Further investigations are needed in the future to improve the accuracy of the impedance measurements and particularly to take into account the effect of the grazing flow. Nevertheless, this work strives to present a first attempt of impedance characterization of such a configuration based on an *in situ* approach.

IV. Numerical approach

In this part, the influence of an impedance wall boundary condition on the amplification of Tollmien-Schlichting waves is numerically analyzed. First, the linear stability equation and the e^N method are briefly introduced. Next, a qualitative study to analyze the impact of the resistance value $R = \text{Re}(Z)$ (imposed by the perforated panel) and the reactance $X = \text{Im}(Z)$ (due to the cavity) on TS instabilities is performed. This theoretical study is performed on a Blasius boundary layer velocity profile, and is also used as a validation of the present numerical approach using existing results available in the open literature. Finally, this study is extended to the experimental set-up presented in section III, where the stability of a spatially growing boundary layer developing on a flat plate with an elliptical leading edge and a succession of solid wall-perforated panel-solid wall is analyzed. In particular, the comparison between measured and

numerically-predicted transition location is performed, and shows reasonably good agreement.

A. Linear Stability analysis

The linear stability theory allows the identification of the unstable modes of the boundary layer. The velocity components (u, v, w), the pressure p and the temperature θ are divided as:

$$q(x, y, z, t) = Q(x, y) + q'(x, y, z, t), \tag{5}$$

where Q represents the steady base flow $(\boldsymbol{U}, \boldsymbol{V})$, P and the temperature T, and q' represents the unsteady three-dimensional infinitesimal perturbation $(\boldsymbol{u'}, \boldsymbol{v'}, \boldsymbol{w'})$, p' and θ'. Since this perturbation is assumed to be modal in the case of natural transition, it is written in the form:

$$q'(x, y, t) = \hat{q}(y) \cdot \mathrm{e}^{-\alpha_i x} \cdot \mathrm{e}^{i(\alpha_r x + \beta z - \omega t)} + c.c., \tag{6}$$

where $c.c.$ denotes the complex conjugate, $-\alpha_i$ is the dimensionless growth rate, α_r is the dimensionless longitudinal wave number, β the spanwise wave number and ω is the dimensionless angular frequency. They are defined with respect to their dimensional starred counterparts by:

$$\alpha = \alpha_r + i\alpha_i = \alpha^* \delta_1, \tag{7}$$

$$\beta = \beta_r + i\beta_i = \beta^* \delta_1, \tag{8}$$

$$\omega = \frac{2\pi f^* \delta_1}{U_e}, \tag{9}$$

where f^* is the mode's dimensional frequency and δ_1 is the boundary layer displacement thickness. A mode is amplified for $\alpha_i < 0$ and it is damped otherwise. At low velocity, Squire's theorem [24] demonstrates that the most unstable modes are two-dimensional ($\beta = 0$), and are therefore sufficient to predict transition onset. The disturbance field is subjected to the following boundary conditions :

$$\begin{cases} \hat{u} = \hat{w} = 0 & \text{at} \quad y = 0 & \text{no slip condition at the wall,} \\ \hat{v} = f(\omega, \hat{p}) = \frac{1}{Z_{\text{stab}}(\omega)} \cdot \hat{p} & \text{at} \quad y = 0 & \text{impedance condition at the wall,} \\ \hat{u} = \hat{v} = \hat{w} = \hat{p} \to 0 & \text{at} \quad y \to \infty & \text{disturbances bounded } \textit{far away} \text{ from the wall.} \end{cases} \tag{10}$$

The classical boundary condition for a rigid wall (no perforations) is written $\hat{v} = 0$ at $y = 0$. In order to take into account the influence of wall impedance on the amplification of the boundary-layer instabilities, this condition is replaced by $\hat{v} = \frac{\hat{p}}{Z_{\text{stab}}}$, Z_{stab} being the dimensionless impedance used for stability computations, deduced from (3), which

can written as:

$$Z_{\text{stab}}(\omega) = Z(\omega)\frac{\rho_0 c_0}{\rho_e U_e} = \frac{\hat{p}(\omega)}{\hat{v}(\omega)}. \tag{11}$$

After introducing the perturbations into the linearized compressible Navier-Stokes equations, a general eigenvalue problem is obtained where the longitudinal wavenumber α is factored out in the right-hand side of the equation and represents the general eigenvalue to be determined :

$$\mathcal{A}\hat{\boldsymbol{q}} = \alpha\mathcal{B}\hat{\boldsymbol{q}}. \tag{12}$$

The eigenvector $\hat{\boldsymbol{q}}$ corresponds to $\hat{\boldsymbol{q}} = (\hat{u}, \hat{v}, \hat{w}, \hat{p}, \hat{\theta})$ and $\mathcal{A}$ and $\mathcal{B}$ are matrices whose coefficients depend on mean flow values and derivative matrices.

The dispersion relation (12) is solved using spectral differentiation of the $\mathcal{A}$ and $\mathcal{B}$ matrices discretized on the Chebishev-Gauss-Lobatto collocation points. The eigenvalue α is determined ny a Newton shooting method.

The total amplification of each unstable mode is computed using the N-factor method developed by van Ingen [1] and Smith and Gamberoni [2]. Consider a given mode of initial amplitude A_0 at the critical abscissa x^*_{cr} that amplifies up to an amplitude A at an abscissa x^*: for each mode whose amplification is exponential, a n-factor is given by

$$n(x^*, f^*) = \ln\frac{A}{A_0} = \int_{x^*_{\text{cr}}}^{x^*} -\alpha_i(\xi, f^*)\,\mathrm{d}\xi. \tag{13}$$

The n-factors of several modes are computed and the envelope curve given by

$$N(x^*) = \max_{\forall f^*}(n(x^*, f^*)). \tag{14}$$

The transition to turbulence takes place at a position x^*_{T} for which the N-factor reaches the transitional N-factor noted N_T.

B. Sensitivity on stability results with different impedance boundaries

In this paragraph, a parametric study of wall impedance on the boundary-layer instabilities is performed with the objective to identify the effects of a purely imaginary impedance (reactance from cavity effect) or a purely real impedance (resistance from perforated plate effect). The study is performed on the theoretical Blasius boundary layer. When possible, the results are compared to the existing ones in the literature and are used as a validation of the current numerical approach.

The neutral curves ($\alpha_i = 0$) delimiting the unstable region is plotted in the plane defined by the Reynolds number based on displacement thickness Re_{δ_1} and the dimensionless angular frequency ω in the so-called stability diagram

represented in Figure 11. These neutral curves as well as the maximum amplification rate ($\min \alpha_i$) are plotted for wall impedance values $Z = 5, 10$ and 20, as well as a standard solid wall ($Z \to \infty$, referred to as 'Blasius' in the caption). Close to the flat plate leading edge, *i.e.* at low Re_{δ_1} values, $\alpha_i > 0$ outside of the region delimited by the neutral curve, indicating that the boundary layer is stable. The Reynolds number below which all the instabilities are damped is called the critical Reynolds number. Moving downstream from the leading edge, the boundary layer gets thicker and Re_{δ_1} increases so that some frequencies become unstable. The critical Reynolds number decreases from $\mathrm{Re}_{\delta_1} = 520$ ($Z \to \infty$) to $\mathrm{Re}_{\delta_1} = 181$ ($Z = 5$) while the range of unstable frequencies widens. Additionally, as the wall impedance decreases, the maximum amplification rate (corresponding to the minimum value of α_i) increases, while shifting to higher $\mathrm{Re}_{\delta 1}$, indicating that a real impedance wall condition promotes the amplification of boundary-layer disturbances.

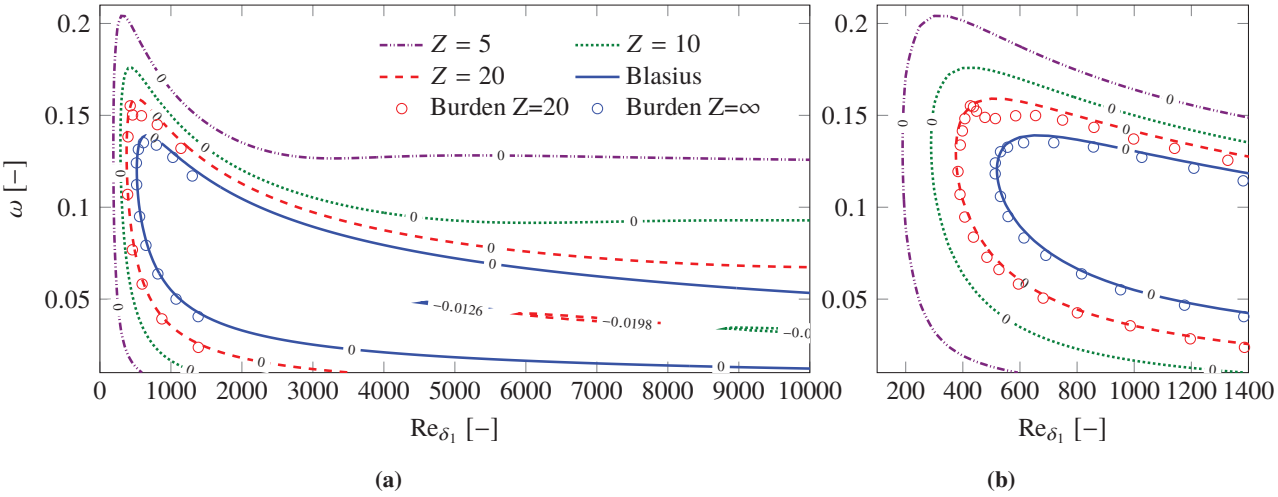

Fig. 11 Stability diagram including the neutral curve ($\alpha_i = 0$) and the maximum amplification rate ($\min \alpha_i$) for a pure real impedance boundary-condition: resistive effect of the perforated panel.

The stability diagram obtained for a purely imaginary impedance $Z = -20i, -5i, 5i$ and $20i$ is shown in the Figure 12. A positive reactance destabilizes the lower branch (referred as 'Branch I' on the figure) of the stability diagram, while it has a stabilizing effect on its upper branch ('Branch II'). A negative reactance will have exactly the opposite effects. The maximum amplification rate remains almost constant.

The same trend has been observed by Choudhari [17] as well as Carpenter and Porter [15] who suggested the possibility of using passive porous walls to control the boundary layer. Carpenter and Porter [15] introduced the admittance $Y = 1/Z$ in the form:

$$Y = |Y|\, e^{i\varphi}, \tag{15}$$

where φ reflects that the flow through the pore is usually out of phase with the driving pressure. The variation of α_r and α_i with φ, are plotted (and compared to our results for validation purpose) in Figure 13 and show that a pure impedance value ($\varphi = 0$ or $90°$) reduces the amplification rate of Tollmien-Schlichting waves. Nevertheless, moving from these

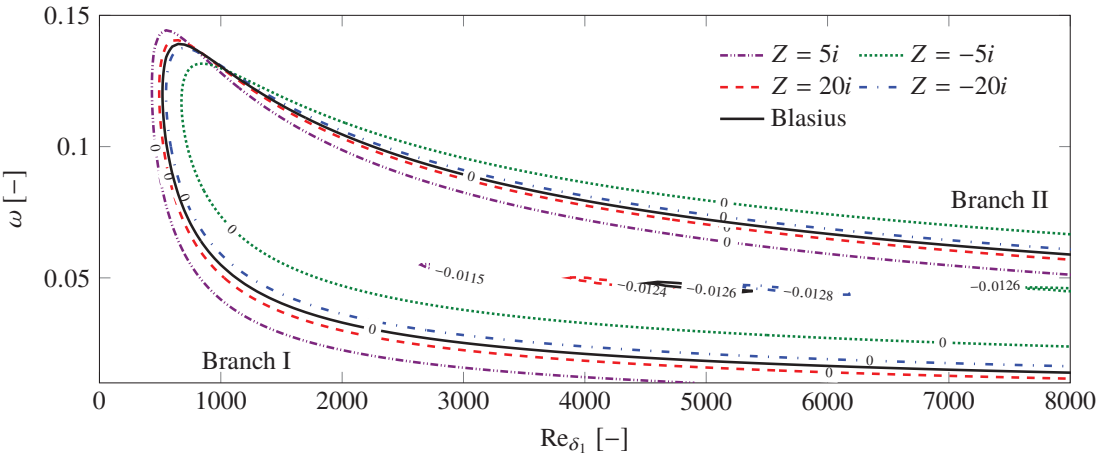

Fig. 12 Stability diagram including the neutral curve ($\alpha_i = 0$) and the maximum amplification rate ($\min \alpha_i$) for a pure imaginary impedance boundary-condition (reactance). Effect of the cavity.

two points, *i.e.* $\mathrm{Re}(Z) \neq 0$, wall impedance enhance the amplification rate. For real impedance value $\varphi = 0$, the strong destabilizing effect is recovered.

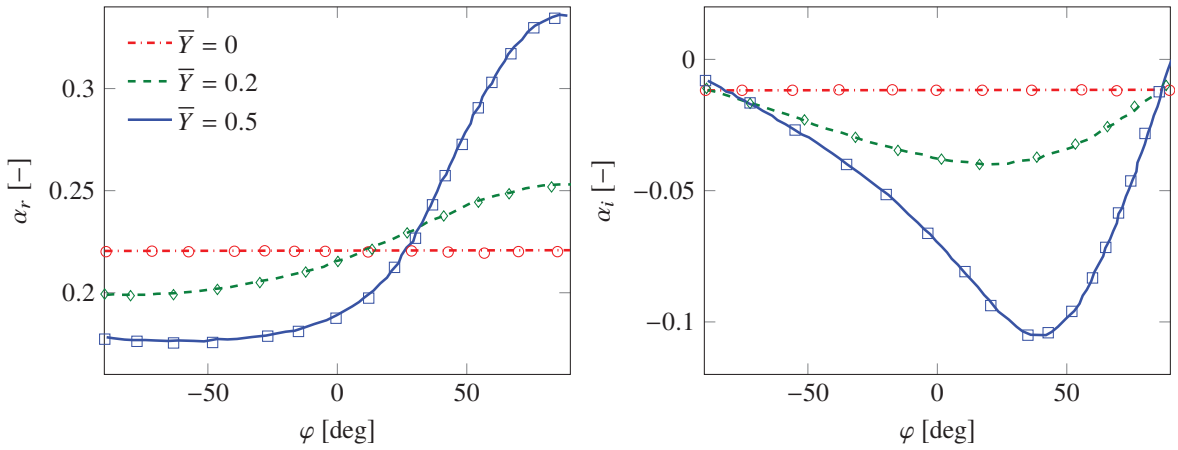

Fig. 13 Variation of (a) α_r and (b) α_i with the phase of admittance for $F = 30 \times 10^{-6}$ and $\mathrm{Re}_{\delta_1} = 2240$ (corresponding to $\omega = 0.0672$). Lines: present numerical code, Symbols: results from Carpenter and Porter [15] for $\overline{Y} = 0$ (○), $\overline{Y} = 0.2$ (◇) and $\overline{Y} = 0.5$ (□).

In the same way, physical configurations do not match the pure imaginary impedance value. In the next section, effective impedance values measured on the flat plate model with the perforated panels mounted over the plenum are use to impose the wall boundary condition that couples the normal velocity fluctuation v' and the pressure fluctuation p'. This value strongly depends on the frequency of the boundary layer instabilities. Moreover, the spatial development of the boundary layer seeing successively a solid wall followed by a perforated panel and a solid wall again and subjected to a non-zero pressure gradient in the leading edge region is taken into account in the computation. This numerical

stability analysis provides the evolution of the so-called N-factors, which are then used to predict the transition location.

C. Impedance effect on the transition onset: experimental set-up configuration

In order to reproduce numerically the experimental results of section II.C, the N-factor envelope (14) is computed while taking into account the measured impedance boundary condition. Over regions of the flat plate where the wall is solid, the classic hard-wall boundary condition $v' = 0$ is applied in the stability calculations. On the other hand, over the perforated panel area between $188 < x < 632$ mm , the measured impedance values (section III.C) are used in the calculations. In order to obtain the N-factor envelope curve, several frequencies are considered. Consequently the impedance boundary condition, which depends on the frequency, is modified accordingly based on the experimental measurement (see Figures 9 and 10). The chosen approach is a simplified approach, which neglects the impedance discontinuities that occur when going from a hard wall condition to a impedance wall condition and *vice versa*.

The envelope curves for the three panels P_0, P_1 and P_2 are plotted in Figure 14. The value of the transitional N-factor N_T is obtained from the experimental results of [5]: for the solid panel (without porosity), the experimental transition location is $x_T^* = 740$ mm and corresponds to the value $N_T = 6.28$. By intersecting this value of N_T on the envelope curves, we get the numerical transition locations listed in the Table 2 as well as the corresponding Tollmien-Schlichting frequencies.

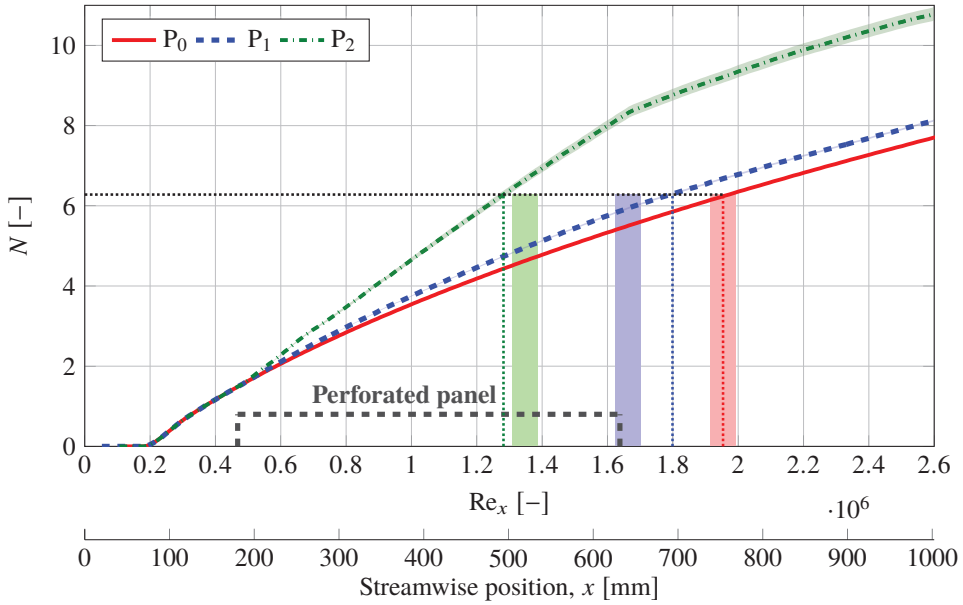

Fig. 14 N-factor curves and transition onset location (vertical color bands stand for hot-wire measurements).

In Figure 14, the experimental transition locations are represented by the vertical color bands to account for uncertainty. The transition position predicted using the impedance value for the P_2 panel with the highest porosity agrees closely with the experimental results.

Table 2 Transition positions according to the perforated plate porosity.

Panel	x_T^* num. [mm]	x_T^* exp. [mm]	Re_{x_T} num. [−]	f_T^* [Hz]	$Z(f_T^*)$ [−]
P_0	740	[725 − 755]	1.95×10^6	600	$+\infty$
P_1	680	[615 − 645]	1.79×10^6	637	$23.5 + 1.2i$
P_2	486	[495 − 525]	1.28×10^6	766	$3.1 + 1.7i$

Regarding the results on P_1 panel with weakest porosity, one can notice that the prediction of the e^N approach does not fully agree with the experimental results. Nonetheless, the considered panel has a high resistance since the holes are small and the porosity is rather low: the P_1 panel nearly behaves like a hard wall, and uncertainty on its impedance measurement is important. The modification of the amplification is thus weaker ; however, considering the impedance of the panel, the onset of the transition is shifted upstream, agreeing with the measurements in the general trend.

Presently, one can also notice that the transition position obtained with the experiments is located at the junction between the perforated and solid walls. A first explanation could be simply a surface defect due to a misplacement of the perforated panels. This explanation can be disproved since the effect of the perforated panels on transition was shown by comparing the full rigid configuration with the perforated panel configuration with tape under the perforated panel: the two transition locations were therefore identical. A more complex explanation of this disagreement for P_1 panel could be the non-local effect of the impedance discontinuity which is not taken into account in the selected mathematical formulation. Indeed, an impedance discontinuity could increase the amplification rate of the considered TS mode. More specifically, the N-factor envelope curve can be shifted to a higher value and thus reach the transition onset threshold value. This discrepancy highlights the limitation of the present approach, which is local, and therefore unable to take into account a possible effect of discontinuity of the wall impedance condition on the hydrodynamics instabilities.

V. Conclusion

This article examines the effect of a perforated panel without suction(initially intended to be used in an HLFC device) as an impedance boundary condition destabilizing the TS waves responsible for the laminar to turbulent transition. Hot-wire measurements showed the promotion of transition when the boundary layer developed over the perforated panels. The present paper therefore conjectures that this effect is due to an impedance condition coupling the wall normal velocity and the pressure fluctuations at the wall and attempts to implement such a model to support this conjecture.

An *in situ* measurement enabled the evaluation the wall impedance of the perforated panels mounted over the chambers in the flat plate model. The impedance measurements were then used as the boundary condition of a local linear stability calculation. The e^N approach was then applied to predict the laminar to turbulent transition onset position. The general trend that with decreasing impedance, transition moved upstream was well captured and particularly good

agreement between experimental and numerical result was found for the low impedance value.

Future work could include taking a global stability approach, in the non-local sense, which could refine the results by taking into account the impedance discontinuities on the flat plate. Other improvements could include experimentally evaluating the wall impedance with grazing flow, which would correspond more closely to the testing conditions. Additionally, the ultimate purpose of such a set-up being the application of wall suction through the perforated panel for the purpose of HLFC of a boundary layer, modeling a bias flow (rather than a grazing flow) could significantly alter the impedance value and could improve the model accuracy. Parametric experimental studies of such phenomena could allow to develop an impedance model of perforated/porous panel that could be used to guide the design of suction flow control systems.

Appendix

A. Evaluation of hot-wire measurement uncertainty

Systematic uncertainty ΔU, which gives a measure of the maximum fixed error that occurs for each measurement, was evaluated using two methods. The first approach is primarily based on the procedure laid out by Yavuzkurt 1984 that uses the classic experimental uncertainty propagation. The contributions to ΔU can be attributed to two sources. The first source is the uncertainty ΔU_1 in the instruments used for hotwire calibration: a Pitot-static tube and an MKS gauge pressure transducer (± 0.3 Pa (0.01% FS)) to measure dynamic pressure P_{dyn}; and a T-type thermocouple (± 2.5 K) and a Digiquartz absolute pressure transducer (± 69 Pa (0.01% FS)) to evaluate local flow density. The ΔU_1 parameter is therefore:

$$\Delta U_1 = \frac{1}{2}\sqrt{\left(\frac{\Delta\rho}{\rho}\right)^2 + \left(\frac{\Delta P_{\text{dyn}}}{P_{\text{dyn}}}\right)^2}\,U = \alpha U \tag{16}$$

The second source of uncertainty ΔU_2 is due to the curve-fitting error between the calculated velocity using the calibration curve (U_2) and the one measured with the calibration instruments (U_1):

$$\Delta U_2 = \beta U \quad \text{with} \quad \beta = \sqrt{\frac{\sum_{i=1}^{n}\left(\frac{\Delta U_{\text{fit}}}{U_1}\right)_i^2}{n}} \quad \text{and} \quad \Delta U_{\text{fit}} = U_2 - U_1. \tag{17}$$

The normalized uncertainty $\Delta U/U$ related to the hotwire calibration can therefore finally be expressed as the sum $\sqrt{(\alpha^2 + \beta^2)}$. Yavuzkurt also shows that the uncertainty parameter ΔU evaluated using this method is identical for both the mean and fluctuating velocity. Based on a case study of seven comparable hotwire calibration data sets taken over the course of a year, the maximum ΔU was 1.09%. The uncertainty in the y-direction, *i.e.* the error reported by the Heidenhain LS388 linear encoders used to monitor the hotwire probe location, is given as ± 0.005 mm. Based on these calculations (validated with an alternative approach based on statistical calibration not shown here) and given the

standard figure format, uncertainty can be said to be within symbol size. An example of a figure in the standard format with error bars showing the uncertainty is shown for both mean and fluctuating velocity profiles in Figure 15.

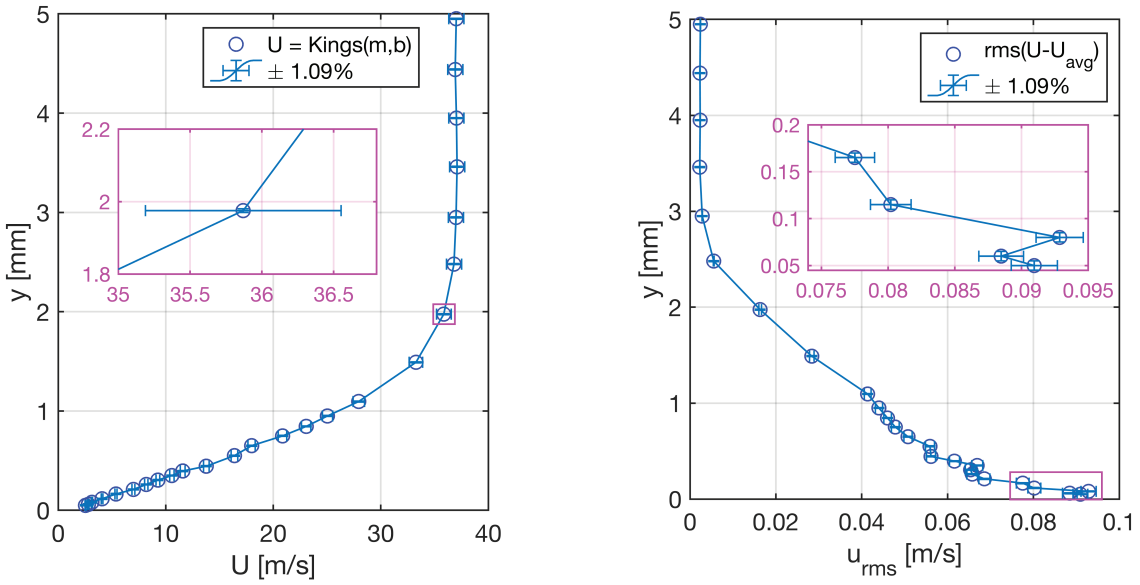

(a) Mean velocity profile with uncertainty. **(b) Fluctuating velocity profile with uncertainty.**

Fig. 15 Mean and fluctuating velocity profiles with uncertainty based on Yavuzkurt.

Acknowledgments

This work has been partly funded within the frame of the Joint Technology Initiative JTI Clean Sky 2, AIRFRAME Integrated Technology Demonstrator platform "AIRFRAME ITD" (contract CSJU-CS2-GAM-AIR-2014-15-01 Annex 1, Issue B04, October 2nd, 2015) being part of the Horizon 2020 research and Innovation framework programme of the European Commission. The authors want to thank Grégoire Casalis from ISAE-Supaero for his advice and fruitful discussions, Estelle Piot for the insight about impedance measurements and grazing flow effect, as well as Jeremie Derré and Olivier Sainges from the acoustics department of Airbus SAS (Toulouse) for the portable impedance tube measurements.

References

[1] van Ingen, J., "A suggested semi-empirical method for the calculation of the boundary layer transition region," Technische Hogeschool Delft, Vliegtuigbouwkunde, Rapport VTH-74, 1956. URL http://resolver.tudelft.nl/uuid:cff1fb47-883f-4cdc-ad07-07d264f3fd10, publieur : Delft University of Technology.

[2] Smith, A., and Gamberoni, N., Transition, Pressure Gradient and Stability Theory, ARC-19322, Douglas Aircraft Company, El

Segundo Division, 1956. URL https://engineering.purdue.edu/~aae519/BAM6QT-Mach-6-tunnel/otherpapers/smith-amo-eN-douglas-es26388-1956.pdf.

[3] Schrauf, G., "Evaluation of the a320 hybrid laminar fin experiment," European Congress on Computational Methods in Applied Sciences and Engineering, ECCOMAS, Barcelona, 2000.

[4] Schrauf, G., "Large-Scale Laminar Flow Tests Evaluated with Linear Stability Theory," Journal of Aircraft, Vol. 41, No. 2, 2004, pp. 224–230. https://doi.org/10.2514/1.9280.

[5] Methel, J., Forte, M., Vermeersch, O., and Casalis, G., "An experimental study on the effects of two-dimensional positive surface defects on the laminar–turbulent transition of a sucked boundary layer," Experiments in Fluids, Vol. 60, No. 6, 2019, p. 94. https://doi.org/10.1007/s00348-019-2741-2.

[6] Chung, J., and Blaser, D., "Transfer function method of measuring in-duct acoustic properties I-theory,II-Experiment," Journal of the Acoustical Society of America, Vol. 68, No. 3, 1980, pp. 907–935. https://doi.org/10.1121/1.384778.

[7] Crandall, I., Theory Of Vibrating Systems And Sound, D. Van Nostrand Company, 1926.

[8] Guess, A., "Calculation of perforated plate liner parameters from specified acoustic resistance and reactance," Journal of Sound and Vibration, Vol. 40, No. 1, 1975, pp. 119 – 137. https://doi.org/10.1016/S0022-460X(75)80234-3.

[9] Elnady, T., and Boden, H., "On Semi-Empirical Liner Impedance Modeling with Grazing Flow," 9th AIAA/CEAS Aeroacoustics Conference and Exhibit, 2003. https://doi.org/10.2514/6.2003-3304.

[10] Melling, T., "The acoustic impendance of perforates at medium and high sound pressure levels," Journal of Sound and Vibration, Vol. 29, No. 1, 1973, pp. 1 – 65. https://doi.org/10.1016/S0022-460X(73)80125-7.

[11] Maa, D. Y., "Potential of microperforated panel absorber," J. Acoust. Soc. Am., Vol. 104, No. 5, 1998, pp. 2861–2866.

[12] Burden, H., "The effect of wall porosity on the stability of parallel flows over compliant boundaries," Ph.D. thesis, Naval Ship Research and Development Center, Washingtonabard, Jan. 1970.

[13] Gaponov, S., "Effect of the properties of a porous coating on boundary layer stability," NASA Technical Memorandum, Vol. NASA TM 75235, 1978.

[14] Lekoudis, S., "Stability of boundary layers over permeable surfaces," 16th Aerospace Sciences Meeting, 1978, p. 203. https://doi.org/10.2514/6.1978-203.

[15] Carpenter, P., and Porter, L., "Effects of Passive Porous Walls on Boundary-Layer Instability," AIAA Journal, Vol. 39, No. 4, 2001, pp. 597–604. https://doi.org/10.2514/2.1381.

[16] Tilton, N., and Cortelezzi, L., "Stability of Boundary Layers over Porous Walls with Suction," AIAA Journal, Vol. 53, No. 10, 2015, pp. 2856–2868. https://doi.org/10.2514/1.J053716.

[17] Choudhari, M., "Effect of nonzero surface admittance on receptivity and stability of compressible boundary layer," NASA STI/Recon Technical Report N, Vol. 95, 1994. URL https://ntrs.nasa.gov/archive/nasa/casi.ntrs.nasa.gov/19950005692.pdf

[18] Heinrich, R., Choudhari, M., and Kershne, E., "A comparison of boundary layer receptivity mechanisms," 1st National Fluid Dynamics Conference, 1988, p. 3758. https://doi.org/10.2514/6.1988-3758

[19] Paluch, B., "Light transmission control technique and correlation with pressure loss characteristics of perforated panels for Hybrid Laminar Flow Applications," Aerodynamic Drag Reduction Technologies, edited by P. Thiede, Springer Berlin Heidelberg, Berlin, Heidelberg, 2001, pp. 71–78. https://doi.org/10.1007/978-3-540-45359-8_9

[20] Gabard, G., "Generalised acoustic impedance for viscous fluids," Journal of Sound and Vibration, Vol. 484, 2020, p. 115525. https://doi.org/10.1016/j.jsv.2020.115525

[21] Kirby, R., and Cummings, A., "The impedance of perforated plates subjected to grazing gas flow and backed by porous media," Journal of Sound and Vibration, Vol. 217, No. 4, 1998, pp. 619–636. https://doi.org/https://doi.org/10.1006/jsvi.1998.1811

[22] Meng, Y., Xin, B., Jing, X., Sun, X., Boden, H., and Abom, M., "Semi-empirical impedance model of perforated plate under grazing flow," 25th AIAA/CEAS Aeroacoustics Conference, 2019. https://doi.org/10.2514/6.2019-2723

[23] Roncen, R., Méry, F., Piot, E., and Simon, F., "Statistical Inference Method for Liner Impedance Eduction with a Shear Grazing Flow," AIAA Journal, Vol. 57, No. 3, 2019, pp. 1055–1065. https://doi.org/10.2514/1.J057559

[24] Squire, H. B., and Southwell, R. V., "On the stability for three-dimensional disturbances of viscous fluid flow between parallel walls," Proceedings of the Royal Society of London. Series A, Containing Papers of a Mathematical and Physical Character, Vol. 142, No. 847, 1933, pp. 621–628. https://doi.org/10.1098/rspa.1933.0193